

Physics Informed Deep Unfolded Full Waveform Inversion for Edema Detection

Ruizhi Zhang*, Yhonatan Kvich*, *Graduate Student Member, IEEE*, Rui Guo, *Member, IEEE*, Oded Cohen, Yonina C. Eldar, *Fellow, IEEE*

Abstract—Edema is a potential indicator of underlying pathological changes. However, its low-contrast signature is often masked in conventional B-mode imaging by strong scatterers, making reliable detection challenging. Ultrasound (US) provides a non-invasive, non-ionizing, and cost-efficient imaging option that is widely used. Conventional techniques, which rely on beamforming, often lack sufficient physical interpretability. Quantitative US (QUS) can estimate physical properties such as the speed of sound (SoS) and density by solving a physics-based inverse problem directly on the measured US wavefields, i.e., the raw per-element channel data (CD), to recover their spatial distribution. However, state-of-the-art physics-based inversion methods, including full waveform inversion (FWI) and model-based quantitative radar and US (MB-QRUS), are computationally intensive and susceptible to local minima, which constrains their clinical utility. We introduce deep unfolded FWI (DUFWI), a physics-faithful unfolded iterative inversion method that exhibits FWI-like refinement behavior while learning the update rule from data, requiring only a small number of iterations for real-time SoS reconstruction. Across both simulated datasets and hardware measurements acquired with a Verasonics US system, the DUFWI significantly outperforms classical FWI and MB-QRUS in reconstruction quality while maintaining high computational efficiency. These results demonstrate real-time edema diagnosis in both simulation and hardware experiments, with phantom-based validation using cylindrical rods, supporting practical deployment under typical US imaging setting.

Index Terms—ultrasound, full waveform inversion, deep unfolding, medical imaging, model-based networks.

I. INTRODUCTION

Arm (upper-limb) edema is the abnormal accumulation of fluid within arm tissue. Timely detection and grading of disease severity guide treatment and enable longitudinal monitoring [1]. Ultrasound (US) is well suited to arm-edema diagnosis and follow-up because it is non-invasive, non-ionizing, portable, and cost-efficient, allowing bedside and repeated assessments [2], [3]. US images are formed from channel data (CD), the raw echo signals recorded on multiple receives. These echoes are produced by the medium in response to sequences of acoustic pulses transmitted from multiple transducer elements [4].

* Equal contribution. Ruizhi Zhang is with University of Electronic Science and Technology of China, China, and also with Faculty of Math and Computer Science, Weizmann Institute of Science, Israel. Yhonatan Kvich, Rui Guo, Oded Cohen and Yonina C. Eldar are with Faculty of Math and Computer Science, Weizmann Institute of Science, Israel.

This research was supported by the Israel Science Foundation (grant No. 3805/21), within the Israel Precision Medicine Partnership (IPMP) program, by the European Research Council (ERC) under the European Union's Horizon 2020 research and innovation program (grant No. 101000967), as well as by Israel Science Foundation (grant No. 536/22).

Conventional B-mode edema assessment relies on beamforming (BF), where received signals from multiple transducer elements are time-aligned and coherently summed with appropriate apodization to enhance echoes from focal regions while suppressing off-axis noise [5]. While effective for structural visualization, BF does not explicitly model tissue acoustic properties that are directly affected by fluid content, such as speed of sound (SoS) and density. As a result, US-based tissue assessment remains limited in specificity and quantitative comparability across patients and time, including for edema [6].

Quantitative US (QUS) addresses these limitations by estimating tissue-specific acoustic parameters including SoS and density [7]. These parameters are mechanistically linked to water content and microstructure, providing biomarkers for more sensitive edema detection, objective grading, and standardized longitudinal tracking. A QUS-based assessment of limb lymphedema is introduced in [8], by using subcutaneous thickness and shear-wave-derived stiffness to distinguish the affected limb from the contralateral limb. Beyond edema, QUS has demonstrated utility in cancer detection, tissue characterization, bone analysis, and rapid stroke imaging [9]–[11].

In a widely used QUS approach, tissue property estimation is formulated as an inverse problem, in which a physically forward model of acoustic wave propagation links spatially varying parameters to the CD. Given CD, spatial parameter maps are estimated by minimizing a regularized data misfit between measured and simulated responses, which yields a nonlinear inverse problem [12]. Full-waveform inversion (FWI) employs gradient-based optimization to reconstruct properties such as SoS and density, which originated from geophysics and then adapted to medical US [13]. Despite its promise, FWI remains computationally demanding and is fundamentally limited by the severe nonlinearity and ill-posedness of the underlying inverse problem, which slows reconstruction and risk convergence to local minima. These challenges limit the application of FWI in medical imaging.

Recently, deep learning methods have been proposed to solve the nonlinear inverse problem in US imaging, enabling real-time reconstructions and reducing the risk of convergence to local minima [14]. By incorporating the wave-equation forward operator, these networks are guided by the explicit physics model, yielding more accurate reconstructions with fewer trainable parameters [15], [16]. For instance, in [17], each finite-difference time-domain (FDTD) time-step is implemented as a recurrent neural cell whose convolutional kernels enforce the acoustic wave equation, enabling SoS reconstruction by back-propagating the data misfit. However, such

methods may exhibit training instability due to the dependence on partial differential equations during backpropagation and demand fine discretizations. In addition, several model-driven deep learning frameworks have been proposed [18]–[20], but they often exhibit degraded convergence under discretization constraints and cannot fully utilize the domain knowledge.

Alternatively, deep unfolding (DU) has recently attracted considerable attention as a powerful tool for solving inverse problems [21]–[24]. By unfolding a conventional iterative algorithm into a finite sequence of trainable layers, DU seamlessly integrates physics-based modeling with data-driven learning [25]–[28]. Examples include the learned primal-dual framework for tomographic reconstruction [29] and unfolding for general imaging tasks [30]. Building on these advances, physics-informed DU has been proposed that embeds physical constraints directly into the network architecture [31], [32]. In the context of US imaging, DU methods have likewise shown great promise for quantitative reconstruction. Notably, the model-based quantitative radar and US (MB-QRUS) approach in [33] operates directly on raw CD and embeds the explicit acoustic forward model into a network, using a learned gradient-descent update within a single unfolded iteration to recover physical property maps. However, a key conceptual advantage of unfolding iterative physics-based inversion is the ability to exhibit iterative refinement. Although MB-QRUS offers high computational efficiency, its reliance on a single iteration may limit its ability to capture fine structural details.

Motivated by the work in microwave imaging [34], we propose a deep unfolded FWI (DUFWI) framework tailored to inverse US, with the goal of preserving the FWI-like iterative correction while learning the update rule, enabling real-time reconstruction with only a few iterations. In our approach, each unfolded iteration uses a neural update module that takes the data-fidelity gradient, computed from full-bandwidth time-domain waveforms, to form an update. This methodology maintains a strong link to the physical knowledge while allowing the update rule to be learned from data by the network. For training efficiency, we adopt a lightweight block-wise training strategy that avoids backpropagating through the full unfolding iteration chain and the associated forward operators. Instead, each iteration is trained as a local subproblem, which substantially reduces both training memory consumption and runtime. After training, the network predicts the SoS update at each iteration based on the data-fidelity gradient.

We evaluate our method on three types of data: (i) SoS maps that are based on MNIST shapes, where the SoS values were chosen to match those observed in real tissues, (ii) clinically motivated simulations of a human arm with or without edema, and (iii) hardware measurements on a tissue-mimicking phantom. In numerical and hardware experiments, DUFWI achieves better performance than classical FWI and MB-QRUS, and requires much fewer iterations than classical FWI. These results highlight the efficiency of our approach, making it a promising solution for practical real-time QUS applications. While this paper focuses on edema detection, we emphasize that the underlying inverse task is general and can yield rich quantitative information across diverse applications.

Preliminary work and results were presented in [35]. Herein,

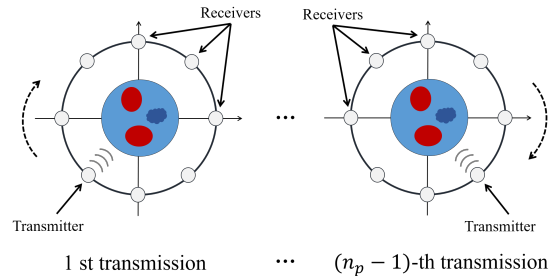


Fig. 1. A typical 2-D measurement setup for edema diagnosis, illustrating a target arm surrounded by a circular array of transducers.

we introduce the full derivation of DUFWI, evaluate the method under broad testing scenarios, and provide a detailed analysis of its advantages. In addition, we design a dedicated measurement system, acquire real CD from a tissue-mimicking phantom, and apply existing inverse methods to these hardware measurements to validate the method beyond simulation. We further describe the implementation details, the clinically motivated dataset, and the hardware evaluation results.

This paper is organized as follows: Section II formulates the forward model and the associated inverse problem, and reviews conventional FWI and MB-QRUS. Section III presents our DU approach to FWI. Section IV details our designed hardware system used to evaluate performance under realistic conditions. Numerical and hardware results are shown in Section V and Section VI, respectively. Section VII offers concluding insights and discusses potential future directions.

II. FOUNDATIONS AND PROBLEM STATEMENT

A. Forward Modeling

In this work, we consider an US imaging system with a circular transducer array of n_p transducer elements. Each element can act as both a transmitter and a receiver. We introduce a sequential transmission scheme, in which a single transducer acts as the transmitter while a subset of other elements of size n_R serves as receivers ($n_R \leq n_p$); the receiver subset can change between transmissions. Each element transmits once, yielding n_p transmission in total and $n_p \times n_R$ received signals. This configuration allows for comprehensive spatial sampling and improved resolution through the integration of multiple independent measurements. The goal of this paper focuses on reconstruction of SoS within the scanned medium, which provides clinical information. A typical 2-D setup for US imaging is illustrated in Fig. 1.

The scattering field, denoted by $u(t, x, z)$, changes in space and time and is related to the physical properties of the scanned medium by the wave propagation equation. For US, the wave propagation equation is expressed as [36]

$$\begin{aligned} c_0^2 \rho_0 \left(\frac{\partial}{\partial x} \left(\frac{1}{\rho_0} \frac{\partial u}{\partial x} \right) + \frac{\partial}{\partial z} \left(\frac{1}{\rho_0} \frac{\partial u}{\partial z} \right) \right) + S \\ = \frac{\partial^2 u}{\partial t^2} + 2D \frac{\partial u}{\partial t} + D^2 u, \end{aligned} \quad (1)$$

where $S(t, x, z)$ represents the source pulse, $c_0(x, z)$ is the SoS of the medium, which is the target parameter in our reconstruction, $\rho_0(x, z)$ is the density of the medium, and $D(x, z)$ is the artificial damping profile used to suppress boundary reflections and allow a finite computational domain. We implement $D(x, z)$ as perfectly matched layers (PMLs)

following the absorbing-boundary formulation in [36], [37], which provides efficient and robust attenuation near the borders. For brevity, in equation (1) we omitted the brackets for S, c_0, D, ρ_0 . We assume that the medium density is constant and set to $\rho_0 = 1000 \text{ kg/m}^3$ [33].

To obtain discrete wave propagation equations, we use a discrete grid with size $n_x \times n_z$ and a discrete form of the time and spatial derivatives [12], [36]. The discrete-time derivative is given by a weighted average of the past time samples, and the discrete-spatial derivative is given by a convolution with the Laplacian or gradient kernel. We denote $\mathbf{U}, \mathbf{S} \in \mathbb{R}^{n_x \times n_z \times n_t}$ as the discrete scattering field and source pulse, respectively, where n_t is the number of discrete-times samples. In addition, we denote $\mathbf{U}[t] \in \mathbb{R}^{n_x \times n_z}$ as the discrete scattering field for the t -th time step (similarly $\mathbf{S}[t]$). After organizing the discrete US wave propagation equation, $\mathbf{U}[t]$ can be written as

$$\begin{aligned} \mathbf{U}[t] &= \frac{\mathbf{2} - \mathbf{D}^2 \Delta_t^2}{\mathbf{1} + \mathbf{D} \Delta_t} \mathbf{U}[t-1] + \frac{\mathbf{D} \Delta_t - \mathbf{1}}{\mathbf{1} + \mathbf{D} \Delta_t} \odot \mathbf{U}[t-2] \\ &\quad + \frac{\mathbf{C}^2 \Delta_t}{\mathbf{1} + \mathbf{D} \Delta_t} \odot (\nabla_D^2 * \mathbf{U}[t-1]) + \mathbf{S}[t]. \end{aligned} \quad (2)$$

Here, \odot is element-wise multiplication, $*$ is the convolution operator, ∇_D is the discrete gradient filter, $\mathbf{1} \in \mathbb{R}^{n_x \times n_z}$ is a matrix of all ones, $\mathbf{2} \in \mathbb{R}^{n_x \times n_z}$ is a matrix of all twos, $\Delta_t \in \mathbb{R}^{n_x \times n_z}$ is a matrix with the value dt for each entry, $\mathbf{C}, \mathbf{D} \in \mathbb{R}^{n_x \times n_z}$ are the discrete SoS, and damping, respectively.

The above forward model describes the transmission of the waveform to the receivers under given physical properties. The pressure field is recorded at the receiver locations. We denote the measured CD for the p -th transmission as $\mathbf{M}[p] \in \mathbb{R}^{n_t \times n_R}$ which consists of n_t time samples and n_R receiving channels. For notational convenience, the forward model for the p -th transmission is written as

$$\mathbf{M}[p] = \tilde{F}_p(\mathbf{C}), \quad (3)$$

where \tilde{F}_p maps the SoS field \mathbf{C} to $\mathbf{M}[p]$ by solving the wave equation and applying the receiver/time-sampling operator. Collecting all transmissions yields

$$\mathbf{M} = \tilde{F}(\mathbf{C}), \quad (4)$$

where $\tilde{F}(\mathbf{C}) \triangleq \{\tilde{F}_p(\mathbf{C})\}_{p=1}^{n_p}$. Our goal is to reconstruct \mathbf{C} from \mathbf{M} , which yields a nonlinear, non-convex, and ill-posed inverse problem in heterogeneous tissues. The following subsections discuss two approaches to solve the inverse problem.

B. Conventional Approach

1) *FWI*: As a physics-based approach, FWI seeks to estimate \mathbf{C} by iteratively minimizing the discrepancy between the observed CD \mathbf{M}_{obs} and $\tilde{F}(\mathbf{C})$ [13], given by

$$C_F := \|\mathbf{M}_{\text{obs}} - \tilde{F}(\mathbf{C})\|_2^2 + \lambda R(\mathbf{C}). \quad (5)$$

where the first term $\|\mathbf{M}_{\text{obs}} - \tilde{F}(\mathbf{C})\|_2^2$ is the data fidelity term that measures the mismatch between the observed data and the simulated measurements, and $\lambda R(\mathbf{C})$ is the regularization term that imposes prior constraints to the solution space [38]. In many practical settings, $R(\mathbf{C})$ is chosen to be non-smooth (e.g., total variation or other ℓ_1 -type penalties), so the overall optimization problem can be handled by operator-splitting

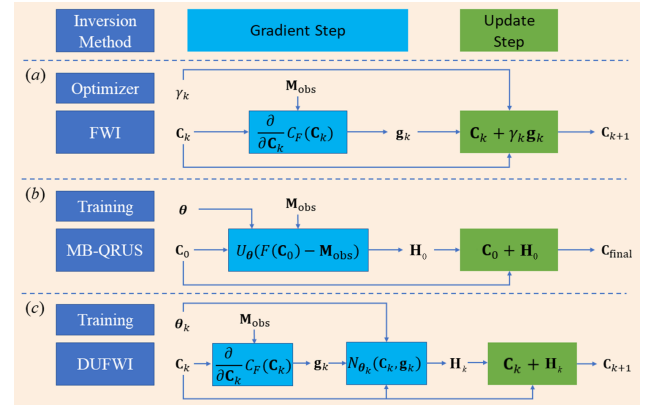


Fig. 2. Visual comparison of the gradient update of three inverse methods: (a) FWI, (b) MB-QRUS, (c) DUFWI.

schemes such as ADMM, where the regularization is enforced via proximal updates rather than explicit gradients [39]. Within this framework, the main computational cost lies in computing the gradient of the data fidelity term with respect to the SoS map. Given a current SoS estimate at iteration k , the gradient of the data-fidelity term is denoted as

$$\mathbf{g}_k := \frac{\partial}{\partial \mathbf{C}_k} \|\mathbf{M}_{\text{obs}} - \tilde{F}(\mathbf{C}_k)\|_2^2. \quad (6)$$

Based on the computed gradient at the k -th iteration \mathbf{g}_k , the SoS map is iteratively updated by

$$\mathbf{C}_{k+1} = \mathbf{C}_k + \gamma_k \mathbf{g}_k, \quad (7)$$

where γ_k is the step size at the k -th iteration. See Fig. 2(a) for an outline of the FWI method.

Nevertheless, the optimization problem underlying FWI is not only highly non-convex but also computationally intensive due to repeated forward wavefield simulation and the subsequent gradient computation. These algorithms rely solely on local gradient information and are therefore susceptible to being trapped in suboptimal solutions. Due to the strong non-convexity of the problem, convergence often requires hundreds or even thousands of iterations, with each involving both forward wave propagation and gradient computation, making the process time-consuming. Reconstructing a single image may take several hours or even days, and often fails to meet the accuracy demands of practical applications.

2) *MB-QRUS*: To address FWI's high computational burden and susceptibility to local minima, MB-QRUS was introduced in [33] and integrates physics-guided modeling with adaptive learning for faster and more accurate reconstruction. MB-QRUS performs a single update, defined as

$$\mathbf{C}_{\text{final}} = \mathbf{C}_0 + \mathbf{H}_0, \quad (8)$$

where \mathbf{C}_0 corresponds to a uniform SoS map, equal to the value of the background, $\mathbf{C}_{\text{final}}$ is the final estimated SoS map, and $\mathbf{H}_0 \in \mathbb{R}^{n_x \times n_z}$ is the update term. This update is predicted by a U-Net-based network U_θ , which adaptively determines both the update direction and the step size. The network incorporates in its design the physical model of wave propagation (2) to calculate $\tilde{F}(\mathbf{C}_0) \in \mathbb{R}^{n_t \times n_p \times n_R}$ for \mathbf{C}_0 , and uses the data residual $\tilde{\mathbf{M}} = \mathbf{M}_{\text{obs}} - \tilde{F}(\mathbf{C}_0)$ as input to U_θ to predict \mathbf{H}_0 . In addition, \mathbf{C}_0 are also given as input to U_θ . A visual schematic of MB-QRUS is provided in Fig. 2(b).

By embedding physical priors directly into the network design, it strikes a balance between interpretability and learning flexibility. In addition, MB-QRUS operates directly in the CD domain, without requiring explicit transformations into the image domain. However, it may underuse available physical and model-based information due to limited incorporation of physics models, which limit reconstruction quality in highly complex scenarios. Without iterative refinement, the model cannot emulate the core optimization mechanism of FWI and is confined to a single-step estimate, rather than the progressive reduction of data misfit achieved through successive gradient-based updates. As a result, generalization across diverse initializations and heterogeneous tissues can be challenging.

III. DEEP UNFOLDING OF FULL WAVEFORM INVERSION

A. DUFWI Framework

To address the limitations of conventional FWI and single-iteration MB-QRUS, we propose a deep unfolding FWI algorithm, which decomposes the inversion into multiple learnable update steps. Each stage is explicitly modeled by a neural network, which takes as input the SoS estimate from the previous stage along with the corresponding gradient of the data fidelity (6), and produces an updated SoS prediction. These networks are trained sequentially to progressively refine the SoS estimate, leading to improved training stability.

Let \mathbf{C}_k and \mathbf{C}_{k+1} denote the SoS map estimates at the k -th and $(k+1)$ -th iterations, respectively. The update at the k -th iteration is defined as

$$\mathbf{C}_{k+1} = \mathbf{C}_k + \mathbf{H}_k, \quad (9)$$

where the update term \mathbf{H}_k is predicted by an iteration-dependent convolutional neural network N_{θ_k} with learnable parameters θ_k that takes the current estimate \mathbf{C}_k and the data fidelity gradient \mathbf{g}_k as inputs, i.e., $\mathbf{H}_k = N_{\theta_k}(\mathbf{C}_k, \mathbf{g}_k)$. The gradient \mathbf{g}_k is computed following the FWI procedure using \mathbf{M}_{obs} and \mathbf{C}_k according to (6). This formulation expresses the inversion as a sequence of learned, gradient-like updates.

The initial input \mathbf{C}_0 is defined as a homogeneous background map, representing a uniform water medium. To address the accumulated complexity of the inversion process, each iteration of the unfolding process uses a network N_{θ_k} with the same architecture and different parameters. This design allows early iterations to make substantial updates, focusing on capturing broader features, while later iterations refine finer structures and make precise adjustments based on the gradient of the data fidelity at each step. Unlike MB-QRUS, which is essentially a single update and may oversmooth fine structures, DUFWI enables iterative learned correction, preserving the FWI mechanism while learning the update rule. A visual illustration of the DUFWI method is shown in Fig. 2(c).

B. Block-wise Training Process

The total training process begins by a training dataset $\left\{ (\mathbf{M}_{\text{obs}}^{(i)}, \mathbf{C}_{\text{gt}}^{(i)}) \right\}_{i=1}^M$, where each pair consists of observed CD and ground truth (GT) SoS maps, and M denotes the total number of training examples. In the k -th iteration, $\tilde{F}(\mathbf{C}_{k-1})$ is first obtained by performing wave propagation using previous estimate \mathbf{C}_{k-1} . The gradients \mathbf{g}_k are precomputed offline for the entire training set by a single pass of the forward

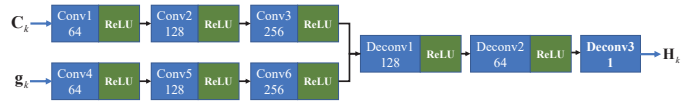


Fig. 3. Illustration of the overall CNN architecture.

operator \tilde{F} and back projection. N_{θ_k} is trained in a supervised manner using the prepared gradient-update pairs. In the k -th iteration, for each training sample i , the network-generated update $\mathbf{H}_k^{(i)} = N_{\theta_k}(\mathbf{C}_k^{(i)}, \mathbf{g}_k^{(i)})$ is added to $\mathbf{C}_k^{(i)}$ as in (9), thereby updating current guess toward the $\mathbf{C}_{\text{gt}}^{(i)}$. Accordingly, the training objective minimizes the discrepancy between $\mathbf{C}_{k+1}^{(i)}$ and the $\mathbf{C}_{\text{gt}}^{(i)}$ by minimizing the mean squared error (MSE) loss

$$\mathcal{L}(\theta_k) = \frac{1}{M} \sum_{i=1}^M \left\| \mathbf{C}_{\text{gt}}^{(i)} - \mathbf{C}_{k+1}^{(i)} \right\|_2^2. \quad (10)$$

In block-wise training, we train the current iteration neural network using the previous estimate and a single physics-based gradient computed with respect to the GT. After training, the network operates in inference mode to produce an updated estimate and computes the data-fidelity gradient from the physical model for each label. These outputs are used to prepare the training dataset for the subsequent iterative block. This avoids gradient backpropagation through the entire cascaded network, substantially reducing the computational overhead of training and enabling larger datasets. Compared to traditional FWI, although the gradient computation remains the same, this learning-based approach significantly accelerates convergence and has the potential to yield more accurate reconstructions.

C. Deep neural network architecture

Following a similar architecture to [34], the input is processed by three convolutional layers with an increasing number of output channels (64, 128, 256), each followed by a ReLU activation. The resulting feature maps are then concatenated and passed through another sequence of three convolutional layers with decreasing output channels (128, 64, 1). Only the first two layers in this second stage apply ReLU activations, while the final convolutional layer acts as the output layer of the network, producing the update \mathbf{H}_k . This output is added to \mathbf{C}_k to generate the updated SoS map, as defined in (9). The convolutional layers employ 5×5 kernels, and zero-padding is applied to preserve the spatial dimensions of the input throughout the network.

D. Deep neural network inference

After the training stage, the DUFWI framework can be applied during the inference within an iterative update process. In the k -th iteration, the gradient of the data misfit with respect to the SoS map is computed and fed into the corresponding trained neural network N_{θ_k} , which produces the update for that iteration. This process continues sequentially over all iterations. DUFWI acts as an operator that maps the current gradient information and existing estimation to a more effective update step. The dominant cost during inference remains the gradient computation from the physical simulator, and the additional cost introduced by the DUFWI neural networks is negligible in comparison. The networks are lightweight, resulting in minimal overhead both in terms of computational complexity and memory usage.

IV. HARDWARE SYSTEM

We demonstrate our algorithm on hardware acquired CD measurements. To achieve this, we employed a Verasonics research US system (Verasonics, Inc., Kirkland, WA, USA) with 16 individually addressable custom immersion transducers (Blatek Industries, USA) arranged in a circular configuration with a 10 cm aperture diameter. The Verasonics platform allows the acquisition and storage of CD.

The arrangement of the transducer elements and the overall hardware system setup are illustrated in Fig. 4 and Fig. 5, respectively. For each transmission, a single element was used as the transmitter, and three elements were used as receivers: the element positioned directly opposite the transmitter and its two adjacent elements. This receive pattern yields $n_R = 3$ channels per transmission. Over $n_p = 16$ transmissions, a total of $n_p \times n_R = 48$ channels are recorded.

The transmission source pulse for each element is a Gaussian pulse with an center frequency of nominally 350 kHz, determined by the transducer hardware. The pulse shape is shown in Fig. 6. For hardware acquisition, the receive waveform is sampled at $f_s = 62.5$ MHz over a $112 \mu\text{s}$ capture window, yielding 7000 uniformly spaced samples per channel. This window exceeds the simulated pulse duration and provides margin for subsequent alignment and spectral calibration.



Fig. 4. Layout of the transducer elements. The circular array consists of 16 evenly spaced elements arranged on a 10 cm diameter ring.

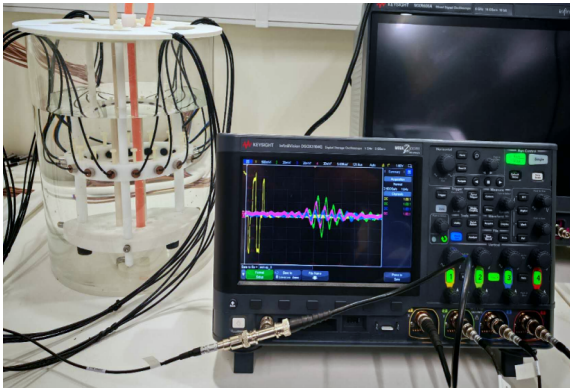


Fig. 5. Overall hardware system: (Left) a transparent water bath housing the circular transducer array; (Right) a Keysight InfiniiVision oscilloscope used only to illustrate example received CD waveforms in real time.

Array calibration is essential for high-performance US imaging because it corrects systematic discrepancies between the acoustic fields produced by individual transducer elements and those predicted by physics-based numerical models. To align simulated and measured CD, we calibrate the transmitted source pulse following [43]. Let $s_{\text{sim}}(t)$ denote the

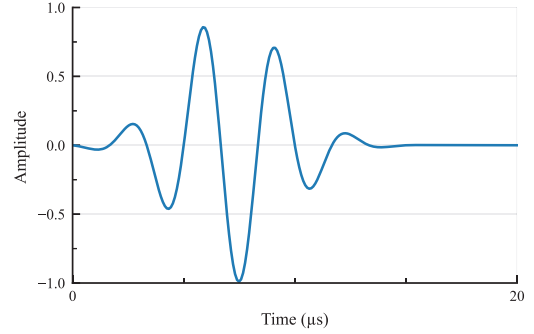


Fig. 6. Transmission pulse waveform from the Verasonics workspace.

simulated source pulse, $r_{\text{sim}}^{(i)}(t)$ the simulated receive CD on the i -th Tx-Rx path, and $r_{\text{hw}}^{(i)}(t)$ the corresponding measured CD. Assuming a linear time-invariant (LTI) propagation/receive chain with frequency response $H^{(i)}(f)$, we have $R_{\text{sim}}^{(i)}(f) = H^{(i)}(f)S_{\text{sim}}(f)$ and $R_{\text{hw}}^{(i)}(f) = H^{(i)}(f)S_{\text{hw}}^{(i)}(f)$, where $S_{\text{sim}}(f)$, $R_{\text{sim}}^{(i)}(f)$, and $R_{\text{hw}}^{(i)}(f)$ denote the Fourier transforms with respect to the ordinary frequency f (in Hz) of $s_{\text{sim}}(t)$, $r_{\text{sim}}^{(i)}(t)$, and $r_{\text{hw}}^{(i)}(t)$, respectively. Eliminating $H^{(i)}(f)$ yields the calibration mapping $S_{\text{hw}}^{(i)}(f) = S_{\text{sim}}(f) \frac{R_{\text{hw}}^{(i)}(f)}{R_{\text{sim}}^{(i)}(f)}$. Consequently, the calibrated time-domain pulse is obtained by applying the inverse Fourier transform to the calibrated spectrum, i.e., $s_{\text{hw}}^{(i)}(t) = \mathcal{F}^{-1}\{S_{\text{hw}}^{(i)}(f)\}$.

In practice, $s_{\text{sim}}(t)$ is chosen as the time derivative of a Gaussian pulse and is discretized with $N_s = 1034$ time samples at a sampling interval $\Delta t_s = 90.243$ ns (total duration $N_s \Delta t_s \approx 93.31 \mu\text{s}$). The simulated receive signals $r_{\text{sim}}^{(i)}(t)$ are generated by numerically solving US wave propagation on a $10 \text{ cm} \times 10 \text{ cm}$ computational domain matched to the transducer array dimensions. The region is discretized on a uniform grid with spacing $\lambda/8$ (where λ is the wavelength), resulting in a 188×188 grid. The Courant–Friedrichs–Lewy (CFL) condition is verified to ensure numerical stability and convergence to a valid PDE solution [42]. A PML of 20 grid points is applied on each boundary. We use a quadratic damping profile within the PML with a target attenuation factor 10^{-3} , yielding a maximum damping coefficient of 1.46×10^6 at the outer boundary. Both the PML thickness and damping parameters are fixed across all experiments.

To improve numerical conditioning and temporal localization, we apply the calibration to the differentiated source wavelet. Specifically, Let $s_{\text{diff}}(t) = \frac{d}{dt}s_{\text{sim}}(t)$, which corresponds to $S_{\text{diff}}(f) = j2\pi f S_{\text{sim}}(f)$ in the frequency domain, where $j = \sqrt{-1}$. We then estimate the equivalent hardware source via $S_{\text{hw}}(f) = S_{\text{diff}}(f) R_{\text{hw}}^{(i)}(f) / R_{\text{sim}}^{(i)}(f)$ and $s_{\text{hw}}^{(i)}(t) = \mathcal{F}^{-1}\{S_{\text{hw}}(f)\}$. The resulting wavelet is zero-mean with a well-localized main lobe and reduced long-duration ringing. Note that differentiation only changes the overall amplitude scaling, since any global scaling of the simulated source also appears in $R_{\text{sim}}^{(i)}(f)$ and cancels in spectral ratio.

At the beginning of the received signals, strong reflections arise from the probe lenses and the phantom interface. Therefore the initial 400 time samples are set to zero to remove such interference, and a moving average filter with a window size of 10 samples is applied, followed by temporal alignment through a shift of 5 samples. A comparison of the raw and

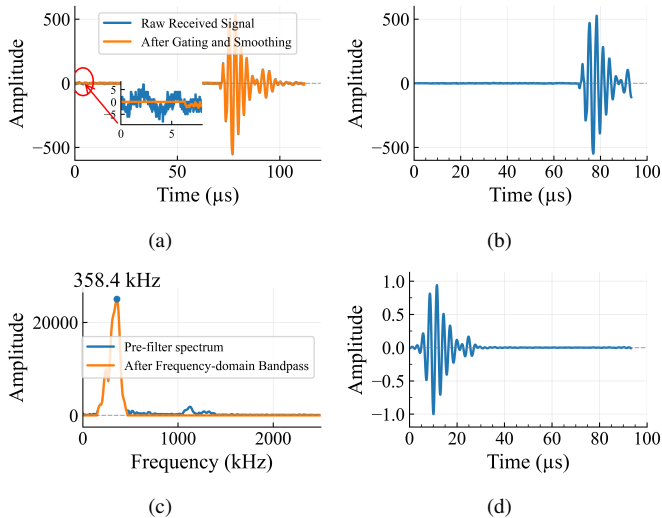


Fig. 7. Illustration of the calibration process. (a) raw vs. gated and smoothed recorded signal; (b) the signal interpolated to the simulation time grid; (c) magnitude spectra before and after the frequency-domain bandpass; (d) normalized calibrated source pulses.

processed measured signal is shown in Fig. 7(a). Subsequently, the filtered signals are digitally resampled (via interpolation) to match the temporal sampling rate of the simulations, as shown in Fig. 7(b). A frequency-domain bandpass filter is then applied to these resampled signals to preserve the main spectral components of the source pulse and attenuate out-of-band noise, as shown in Fig. 7(c).

Finally, the ratio between the measured signal spectrum and the simulated received signal spectrum is computed and multiplied by the simulated source pulse spectrum, which produces an estimate of the hardware source pulse. The calibrated source pulse is recovered by applying the inverse Fourier transform and then peak-normalized to unit magnitude for consistency across channels and to prevent amplitude saturation. The calibrated source are shown in Fig. 7(d). This calibration aligns the simulated and measured CD in both timing and spectrum, which is critical for stable inversion.

V. NUMERICAL RESULTS

The inversion methods described in Section II are first validated on simulated datasets, followed by evaluation on measured hardware data. Specifically, two types of simulated datasets are employed for subsequent evaluations, with the two networks are trained independently.

1) *MNIST dataset*: First, the SoS maps dataset used for training is derived from the MNIST [40]. Reconstructing MNIST digits can be challenging because the cavities (hollow or enclosed regions) within the digits act as resonators, which leads to strong multiple scattering phenomena that increase the nonlinearity of the inverse problem. To prepare this dataset, we load each digit image and apply a sequence of transformations: conversion to tensor (normalizing pixel values to $[0, 1]$), random rotations ($\pm 30^\circ$), translations (± 5 pixels), scaling ($0.8 \times - 1.2 \times$), shear ($\pm 10^\circ$), and random erasing. Each augmented image is then multiplied by a random factor sampled uniformly from $[0.3, 1.2]$, thereby exposing the network to a broad range of SoS contrasts. Next, the image is resized to fit the circular transducer array grid. A final random in-

plane rotation is applied before scaling the image intensities by 666 m/s and adding a bias of 1550 m/s to yield the GT.

2) *Simulated arm dataset*: To evaluate the performance of the proposed method on arm scenario, we generated a simulated arm dataset designed to mimic the cross-sectional profile of a human arm. Each sample is defined on a $10 \text{ cm} \times 10 \text{ cm}$ rectangular domain and contains an elliptical foreground region in which tissue properties are assigned. The outer boundary represents skin. Beneath the skin lies subcutaneous fat. The interior is muscle compartment. Two circular bone regions are placed in the muscle. An optional small elliptical edema region appears in the muscle. To train and evaluate the network, we constructed a single combined dataset that includes both edema-present and edema-absent samples, and the dataset was balanced with a 1 : 1 ratio between the two groups, and the network was trained on this combined set rather than on two separate datasets. Across samples, arms differ in their external contour and their underlying tissue structures, including differences in skin, bone, and edema. The SoS values for each tissue type were selected based on physiological measurements, including muscle (1570–1620 m/s), fat (1420–1450 m/s), skin (1530–1560 m/s), bone (2700–3000 m/s), and edema (1450–1500 m/s) [41].

In training process, the proposed DUFWI framework is unrolled for 5 iterations. At each iteration k , we train the corresponding network N_{θ_k} for 40 epochs using a batch size of 32 and the Adam optimizer [44]. The learning rate for different network in each iteration is set according to the schedule $\eta_k = [1e^{-4}, 1e^{-4}, 5e^{-5}, 1e^{-5}, 1e^{-5}]$. The training loss for DUFWI and MB-QRUS is the MSE. All other training hyperparameters remain fixed across iterations. In addition, we apply an offset-and-normalization to the input SoS map for numerical stability. We subtract 1400 m/s as a soft-tissue reference near the lower end of dataset. Although bone has much larger SoS, the subsequent normalization maps the dynamic range to comparable magnitudes for the network. After the network output, a corresponding post-processing step rescales the output \mathbf{H}_k to keep align with the original units.

All models (DUFWI and MB-QRUS) were trained on a single NVIDIA A40 GPU with 70 GB of memory, and all the experiments are implemented in Pytorch 2.5.1. To assess MB-QRUS on our problem setup, we retrained the network from Section II-B.2 using our SoS maps and forward model, and adapted it to our 16-element circular array configuration. In addition, for the FWI baseline across all experiments, we implement an ADMM-based solver with 200 outer iterations (no stopping criterion) and an ℓ_1 -type regularization applied to the spatial derivatives (total variation regularization). In each iteration, the data-fidelity subproblem is minimized using L-BFGS with learning rate is 1 and iteration is 5 [46], [47].

For each type of simulated dataset, we generate 20,000 SoS maps, partitioned into 16,000 for training and 4,000 for validation. The SoS maps above described are used as the GT. To generate a training dataset $\left\{ \left(\mathbf{M}_{\text{obs}}^{(i)}, \mathbf{C}_{\text{gt}}^{(i)} \right) \right\}$, the observed CD for each example is calculated using the forward model described in Section II-A as $\mathbf{M}_{\text{obs}}^{(i)} = \hat{F}(\mathbf{C}_{\text{gt}}^{(i)})$, which is required by both DUFWI and MB-QRUS. All training

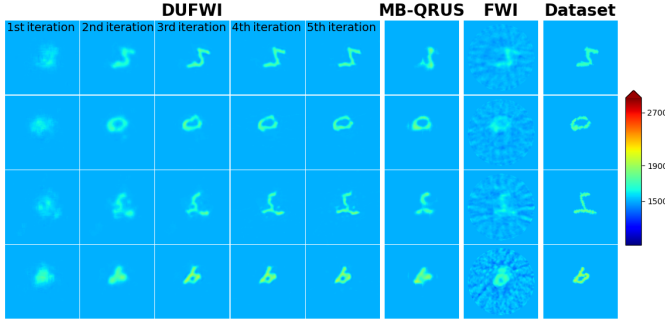


Fig. 8. Reconstructed SoS maps from the MNIST test subset, displayed across several unfolded iterations. This visualization shows the progression and refinement of the SoS maps through multiple iterations.

datasets are noise-free, with additive gaussian white noise being added to the CD during testing under signal-to-noise ratio (SNR) is 30 dB. This setup allows the model to learn the underlying properties from noise-free data during training, while evaluating the robustness to noise during testing.

A. MNIST Dataset Results

Fig. 8 illustrates the reconstructed SoS maps of DUFWI (shown after postprocessing) compared to MB-QRUS, FWI, and GT on four MNIST-based test examples. Across all methods, the initial SoS map C_0 corresponds to a homogeneous water medium. DUFWI reconstructs finer structural details and yields visually more accurate SoS maps than MB-QRUS and conventional FWI. In addition, as illustrated in Fig. 8, it can be observed that DUFWI captures the approximate location of object in the first iteration, constructs its overall shape in the second iteration, and then progressively refines the detailed image features in subsequent iterations. To better quantify the advantages of DUFWI, three metrics are used to evaluate the test-set results: the structural similarity index (SSIM), the peak signal-to-noise ratio (PSNR), and the normalized mean squared error (NMSE) to gauge the accuracy of the reconstructed physical parameters [12], [45]. A full quantitative comparison across iterations appears in Table I. Across all iterations, the proposed DUFWI method consistently outperforms FWI, and in the final iteration it also surpasses MB-QRUS on the quantitative metrics. During the first two iterations, DUFWI exhibits relatively lower metric values, however, in the third iteration, its performance surpasses that of MB-QRUS. In subsequent iterations, DUFWI’s metrics continue to improve, consistent with the behavior illustrated in Fig. 8.

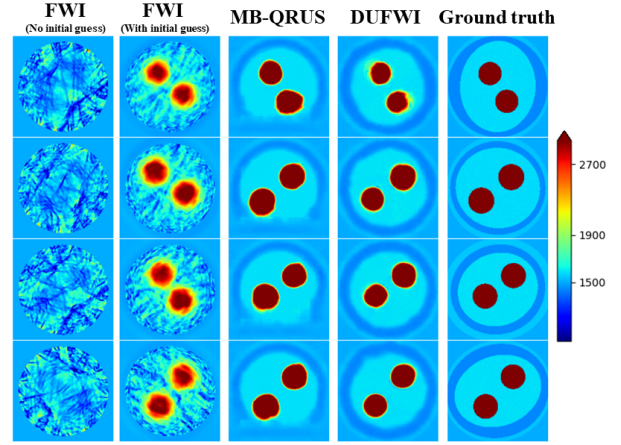
TABLE I

Quantitative comparison on MNIST test data. The quantitative metrics of DUFWI improve with each iteration. Arrows indicate the preferred direction (\uparrow higher is better, \downarrow lower is better).

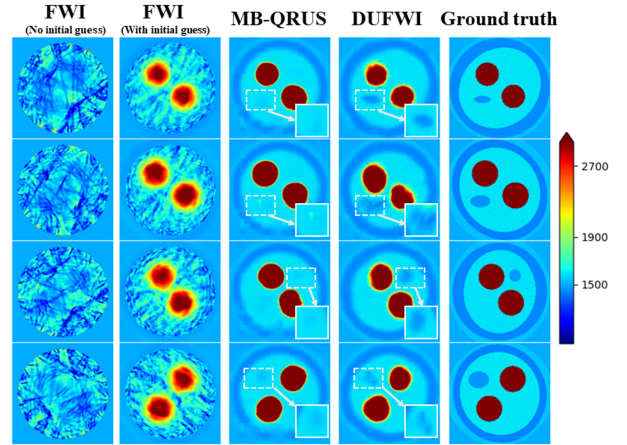
Metric	MNIST Test Data						
	FWI	MB-QRUS	DUFWI				
			1st iter	2nd iter	3rd iter	4th iter	5th iter
SSIM (\uparrow)	0.9409	0.9871	0.9787	0.9833	0.9877	0.9901	0.9916
PSNR (dB) (\uparrow)	38.39	43.41	40.58	43.22	44.59	46.58	47.41
NMSE (dB) (\downarrow)	-33.98	-36.47	-34.13	-35.63	-37.00	-38.01	-38.81

B. Simulated Arm Dataset Results

To further test the effectiveness of the DUFWI in anatomical applications, we evaluate all methods on simulated arm test data with and without edema. Owing to the stronger tissue heterogeneity and SoS contrast in this dataset, conventional FWI stagnate or fail under unfavorable initial conditions. Consequently, we benchmark the proposed DUFWI against



(a) Simulated arm without edema



(b) Simulated arm with edema

Fig. 9. Reconstructed SoS maps of simulated arm examples: (a) non-edema case and (b) edema case. The figure compares the performance of DUFWI with FWI and MB-QRUS.

MB-QRUS and conventional FWI under two complementary initialization strategies: one employs an initial SoS C_0 assuming a homogeneous water medium consistent with DUFWI and MB-QRUS, while the alternative initial guess incorporates approximate bone locations embedded within a water background through Gaussian blurring, leaving the SoS and positions of muscle, skin, and edema unspecified.

Fig. 9 summarizes the reconstructed SoS maps for both scenarios: the non-edema in Fig. 9(a) and the edema in Fig. 9(b). When initialized from a homogeneous water medium, conventional FWI produces severe speckle artifacts, fails to recover the high-speed bone tissue and unable to reconstruct the low-speed skin boundaries or the internal edema region in the edema case. Although the introduction of an initial guess significantly reduces background artifacts and sharpens the bone interfaces, skin boundaries remain blurred and the edema region remains undetectable. The MB-QRUS method yields nearly speckle-free and smooth reconstructions, yet this oversmoothing distorts skin morphology and nearly eliminates visibility of the low-speed edema region, indicating that MB-QRUS may converge to a local minimum.

In contrast, DUFWI employs multiple unfolding iterations that enforce data fidelity together. In the non-edema case, DUFWI clearly resolves bone regions, while in the edema

TABLE II

Quantitative Comparison for the Reconstructed SoS Maps of Simulated Arm Data for Non-Edema Case Shown in Fig. 9(a).

Simulated Arm Data for Non-Edema Case				
Metric	FWI		MB-QRUS	DUFWI
	No Init. Guess	With Init. Guess		
SSIM (\uparrow)	0.5894	0.7187	0.9138	0.9163
PSNR (dB) (\uparrow)	15.4119	20.8215	29.0541	29.4148
NMSE (dB) (\downarrow)	-12.2213	-16.8712	-23.1136	-23.3365

TABLE III

Quantitative Comparison for the Reconstructed SoS Maps of Simulated Arm Data for Edema Case Shown in Fig. 9(b).

Simulated Arm Data for Edema Case				
Metric	FWI		MB-QRUS	DUFWI
	No Init. Guess	With Init. Guess		
SSIM (\uparrow)	0.5853	0.7095	0.8957	0.9059
PSNR (dB) (\uparrow)	15.5052	20.2911	28.8906	29.1282
NMSE (dB) (\downarrow)	-12.1594	-16.7023	-23.9019	-23.8702
LMSE (\downarrow)	526.1629	361.7628	380.9106	255.1932

case, it accurately delineates both high-speed bones and surrounding low-speed tissues. Compared with MB-QRUS, DUFWI better reconstructs low-speed tissues adjacent to bone in the edema scenario, highlighting its potential for medical imaging applications aimed at diagnosing and characterizing abnormal tissues. The quantitative comparison of non-edema case and edema case are provided in Table II and Table III, respectively. In the non-edema case, the proposed DUFWI method outperforms MB-QRUS across all quantitative metrics, demonstrating superior reconstruction accuracy. Additionally, in the edema case, MB-QRUS shows marginally lower NMSE than DUFWI, whereas DUFWI maintains higher SSIM and PSNR. As a global squared-error metric, NMSE is largely driven by the majority non-edema region. Although MB-QRUS produces smoother reconstructions, it tends to over-smooth low-speed regions like edema. We further report local MSE (LMSE) to evaluate the reconstruction accuracy inside the edema region, where DUFWI achieves the lowest LMSE, indicating a more accurate recovery of edema.

Besides, since both DUFWI and MB-QRUS recover high-contrast structures (e.g., bone and skin) comparably well, we further probe the low-contrast edema region in Fig. 10. To diagnose the edema, we introduce a classification procedure for edema detection on reconstructed SoS maps. After excluding bone and skin masks, we apply Gaussian smoothing to the remaining tissue region to suppress high-frequency noise while preserving low-contrast structures. Candidate edema regions are obtained by thresholding the SoS map to the physiologically informed range of 1460–1500, and then 2-D connected-component labeling on the binarized mask is performed, discarding components that fail basic plausibility checks (e.g., minimum area or proximity to excluded bone/skin masks). Finally, for each component we extract a sub-pixel contour and use the resulting closed curves as the edema boundaries. This classification method is performed on both DUFWI and MB-QRUS. Applying this procedure to all test samples, we obtain edema classification quantitative results summarized in Table IV, which show that DUFWI achieves markedly better diagnostic performance for edema classification than MB-QRUS. Specifically, DUFWI achieves 100% precision (no false positives), while maintaining 88% recall, indicating reliable detection of edema cases. In contrast, MB-QRUS attains 88.235% precision but only 0.75% recall,

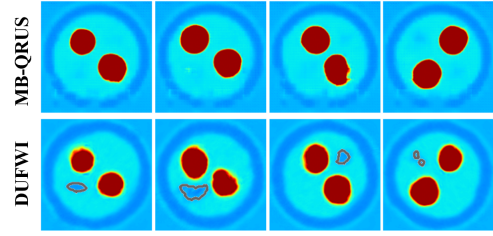


Fig. 10. Classification results for the Simulated Arm Data in Fig. 9(b) obtained by DUFWI (last iteration) and MB-QRUS.

TABLE IV

Edema Detection Performance on the Simulated Arm Dataset (Acc./Prec./Rec for both cases; Dice only for edema cases)

Simulated Arm Dataset for Both Case		
Metric	MB-QRUS	DUFWI
Accuracy (%)	50.325	94.0
Precision (%)	88.235	100
Recall (%)	0.75	88.0
Dice (\uparrow)	0.0355	0.5302

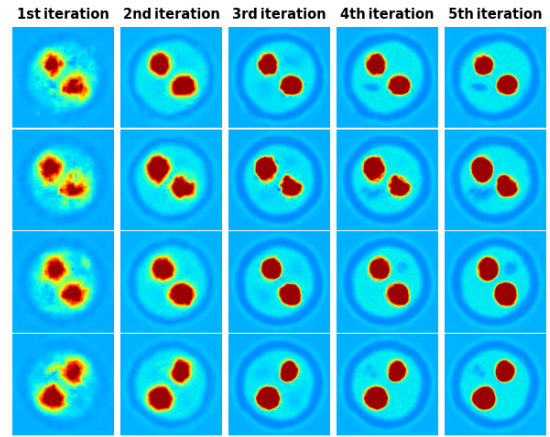


Fig. 11. Reconstructed SoS maps from the simulated arm with edema examples, displayed across 5 unfolded iterations.

indicating a high false negative rate. This is mainly due to oversmoothing of MB-QRUS, which suppresses the low-speed contrast of the edema region. Consequently, its overall accuracy is substantially lower. To complement the sample-level classification results, we further report the Dice coefficient in Table IV to quantify the spatial overlap between the detected edema region and the reference edema mask derived from the GT. MB-QRUS attains a near-zero Dice, indicating negligible spatial overlap with the reference edema region. DUFWI improves the Dice to 0.5302, indicating improved edema localization and boundary delineation. As no visible edema can be observed in the FWI results (Fig. 9(b)), FWI appears ill-suited for edema detection, since it fails to provide discriminative edema-related features. Therefore, we omit the comparison with FWI in Table IV. Overall, DUFWI yields a more reliable edema assessment than MB-QRUS, supported by improved sensitivity and spatial agreement with the GT.

Fig. 11 illustrates the iterative evolution of DUFWI for SoS reconstruction in edema case. During the first two iterations, DUFWI primarily recovers high-contrast anatomical boundaries. Subsequently, DUFWI progressively recovers the low-contrast edema region. This progression indicates that, compared with MB-QRUS, DUFWI is less susceptible to sub-optimal local minima and yields more faithful SoS estimates within and around the edema, beneficial for medical diagnosis.

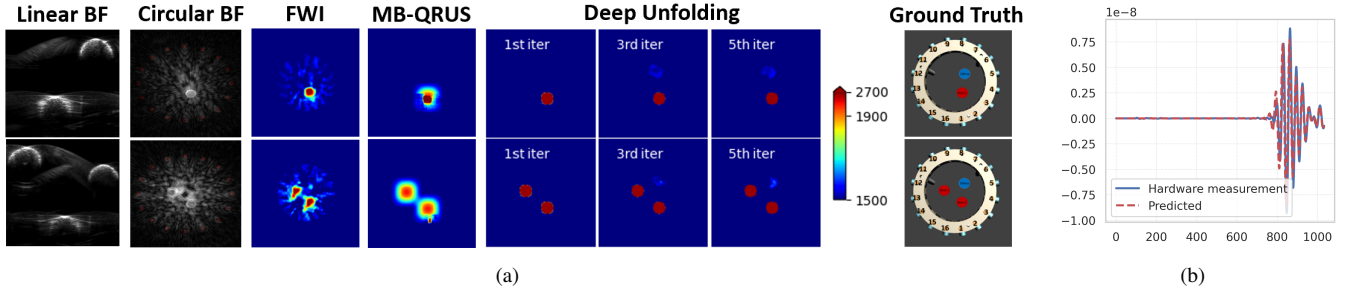


Fig. 12. Hardware results: (a) Reconstructed SoS maps from the measured phantom data. “Bone” rods correspond to high SoS value (≈ 2700 m/s) and “edema” rods correspond to low SoS value (≈ 1588 m/s). (b) Comparison of hardware measurement and DUFWI-based simulated CD.

VI. HARDWARE RESULTS

In this section, we further evaluate DUFWI for practical edema diagnosis using the hardware system described in Section IV. To validate the proposed DUFWI method under realistic conditions using our hardware system, we created a circular phantom dataset. This dataset consists of cylindrical rods immersed in a water bath, each containing 1 to 3 rods (diameter: 1 cm) representing bone (2700 m/s) or edema (1588 m/s). These rods were embedded within a homogeneous water background (approximately 1500 m/s) to create strong acoustic contrast, simulating clinically relevant scenarios. GT rod locations are approximate due to manual placement. During training, we use simulated rods with well-defined boundaries to match the experimental setup, while for testing, we employ real maps to assess the generalization capability of DUFWI. This approach introduces a domain gap between training and testing, challenging the model to accurately reconstruct SoS maps from noisy, real-world data.

We generate 16000 simulated data to train the proposed DUFWI architecture. As described earlier, the arm dataset includes both edema and non-edema cases: the non-edema subset models two bones within a homogeneous soft-tissue background, whereas the edema subset adds an elliptical, low speed region to mimic interstitial fluid accumulation. This design supports anatomically realistic training and evaluation.

Fig. 12(a) illustrates qualitative reconstructions from measured phantom CD of two test phantoms described in IV using linear beamforming from the side (by a different probe), circular beamforming (from the circular CD), the conventional FWI, MB-QRUS, and the proposed DUFWI. Linear beamforming yields broad arc-shaped responses and strong multipath clutter, and returns only an intensity envelope without quantitative estimation such as SoS value. Circular beamforming benefits from a larger effective aperture yet still shows pronounced sidelobes and speckle, moreover, the lack of quantitative mapping and the residual artifacts make edema identification unreliable. In contrast, DUFWI rapidly forms compact and high-contrast spots at the true locations: by the 1st-3rd iterations the targets are clearly localized, and by the 5th iteration the reconstructions are stable with low background energy and minimal ringing. MB-QRUS can only provide a coarse localization of the bone structures and completely fails to identify the edema regions. Conventional FWI produces broader artifacts with blurred peaks and occasional position bias. In addition, FWI used 200 iterations, whereas DUFWI used only 5 iterations. The average runtime was

60 ± 20 minutes for FWI and 15.83 ± 3 seconds for DUFWI, corresponding to an approximate $227\times$ speedup in favor of DUFWI. Quantitative results comparing DUFWI and FWI are summarized in Table V.

TABLE V

Quantitative comparison across all hardware measured data.

Metric	Measured Data						
	FWI	MB-QRUS	DUFWI				
			1st iter	2nd iter	3rd iter	4th iter	5th iter
SSIM (\uparrow)	0.9116	0.9195	0.9814	0.9817	0.9834	0.9840	0.9846
PSNR (dB) (\uparrow)	28.41	28.80	35.04	35.54	35.63	35.65	35.66
NMSE (dB) (\downarrow)	-23.65	-27.98	-30.17	-30.65	-30.76	-30.79	-30.81

As a representative example from the second scenario in Fig. 12(a), Fig. 12(b) compares the hardware-measured CD with the simulated CD from the DUFWI-reconstructed SoS. Prior to the first arrival, both CD remain near the noise. At the onset (around sample index 800), the simulated received signal aligns in time with the measurement. The carrier frequency, envelope shape, and peak amplitude are closely matched, indicating high data consistency between the DUFWI-based results and the physical acquisition.

Overall, DUFWI enables high-quality US reconstructions with a reduced number of iterations, providing real-time quantitative recovery of edema morphology and supporting clinical decisions.

VII. CONCLUSION

The proposed DUFWI framework offers a real-time solution for edema diagnosis. By unrolling a FWI algorithm and replacing each gradient step with a learned correction network, DUFWI reconstructs high-fidelity SoS maps from CD. In extensive 2-D numerical experiments on simulated MNIST, simulated arm datasets, together with measurements on phantom data, DUFWI surpasses classical FWI and the MB-QRUS in reconstruction accuracy. This stems from the model-driven design, which leverages trainable gradient updates to achieve superior efficiency with less computational overhead.

Looking ahead, within the same DUFWI framework, we can recover additional physical properties, such as density and attenuation, by using forward models whose propagation physics explicitly account for these quantities. Future work will validate these extensions on complex, realistic phantom measurements to expand clinical relevance in brain, breast imaging and other clinical settings.

REFERENCES

- [1] C. Pirri, C. Ferraretto, N. Pirri, L. Bonaldo, R. De Caro, S. Masiero, and C. Stecco, “Ultrasound examination of skin, fasciae and subcutaneous tissue: Optimizing rehabilitation for secondary upper limb lymphedema,” *Diagnostics*, vol. 14, no. 24, Art. 2824, 2024.

- [2] C. Pirri, N. Pirri, C. Ferraretto, L. Bonaldo, R. De Caro, S. Masiero, and C. Stecco, "Ultrasound imaging of the superficial and deep fascia thickness of upper limbs in lymphedema patients versus healthy subjects," *Diagnostics*, vol. 14, no. 23, Art. 2697, 2024.
- [3] I. S. Raj, S. R. Bird, and A. J. Shield, "Ultrasound measurements of skeletal muscle architecture are associated with strength and functional capacity in older adults," *Ultrasound in Medicine & Biology*, vol. 43, no. 3, pp. 586–594, 2017.
- [4] T. L. Szabo, *Diagnostic Ultrasound Imaging: Inside Out*. Burlington, MA: Academic Press, 2004.
- [5] B. D. Van Veen and K. M. Buckley, "Beamforming: A versatile approach to spatial filtering," *IEEE ASSP Mag.*, vol. 5, no. 2, pp. 4–24, 1988.
- [6] M. Demirci, C. Sanal, I. Yagci, and G. Akyuz, "Evaluation of elastographic parameters in patients with breast cancer-related lymphedema and examination of their relationship with clinical data," *Lymphatic Research and Biology*, vol. 23, no. 4, pp. 263–271, 2025.
- [7] D. H. Lee, "Imaging evaluation of non-alcoholic fatty liver disease: Focused on quantification," *Clin. Mol. Hepatol.*, vol. 23, no. 4, pp. 290–301, 2017.
- [8] A. V. Polat, M. Ozturk, A. K. Polat, U. Karabacak, T. Bekci, and N. Murat, "Efficacy of ultrasound and shear wave elastography for the diagnosis of breast cancer-related lymphedema," *Journal of Ultrasound in Medicine*, vol. 39, no. 4, pp. 795–803, 2020.
- [9] M. Hopfer, R. Planas, A. Hamidipour, T. Henriksson, and S. Semenov, "Electromagnetic tomography for detection, differentiation, and monitoring of brain stroke: A virtual data and human head phantom study," *IEEE Antennas Propag. Mag.*, vol. 59, no. 5, pp. 86–97, 2017.
- [10] T. Zhang, H. Shi, Y. Cao, H. Zhang, R. Guo, M. Li, F. Yang, and S. Xu, "Attenuation tomography using low-frequency ultrasound for thorax imaging: Feasibility study," *IEEE Trans. Biomed. Eng.*, vol. 71, no. 8, pp. 2367–2378, Aug. 2024.
- [11] H. N. Minh, J. Du, and K. Raum, "Estimation of Thickness and Speed of Sound in Cortical Bone Using Multifocus Pulse-Echo Ultrasound," *IEEE Trans. Ultrason., Ferroelectr., Freq. Control*, vol. 67, no. 3, pp. 568–579, 2020.
- [12] A. Shultzman and Y. C. Eldar, "Nonlinear waveform inversion for quantitative ultrasound," *IEEE Trans. Comput. Imaging*, vol. 8, pp. 893–904, 2022.
- [13] L. Guasch, O. C. Agudo, M.-X. Tang, P. Nachev, and M. Warner, "Full-waveform inversion imaging of the human brain," *NPJ Digit. Med.*, vol. 3, no. 1, 2020.
- [14] M. Ambrosanio, S. Franceschini, V. Pascasio, and F. Baselice, "An end-to-end deep learning approach for quantitative microwave breast imaging in real-time applications," *Bioengineering*, vol. 9, no. 11, 2022.
- [15] N. Shlezinger, Y. C. Eldar, and S. P. Boyd, "Model-based deep learning: On the intersection of deep learning and optimization," *IEEE Access*, vol. 10, pp. 115384–115398, 2022.
- [16] N. Shlezinger, J. Whang, Y. C. Eldar, and A. G. Dimakis, "Model-based deep learning," *Proc. IEEE*, vol. 111, no. 5, pp. 465–499, 2023.
- [17] Y. Hu, Y. Jin, X. Wu, and J. Chen, "A theory-guided deep neural network for time domain electromagnetic simulation and inversion using a differentiable programming platform," *IEEE Trans. Antennas Propag.*, vol. 70, no. 1, pp. 767–772, 2022.
- [18] Y. Ren, X. Xu, S. Yang, L. Nie, and Y. Chen, "A physics-based neural network way to perform seismic full waveform inversion," *IEEE Access*, vol. 8, pp. 112266–112277, 2020.
- [19] M. Heller and G. Schmitz, "Deep learning-based speed-of-sound reconstruction for single-sided pulse-echo ultrasound using a coherency measure as input feature," in *Proc. 2021 IEEE Int. Ultrasonics Symp.*, pp. 1–4.
- [20] J. Liu, et al., "Physical model-inspired deep unrolling network for solving nonlinear inverse scattering problems," *IEEE Trans. Antennas Propag.*, vol. 70, no. 2, pp. 1236–1249, 2022.
- [21] R. Guo, Z. Lin, T. Shan, X. Song, M. Li, and F. Yang, "Physics embedded deep neural network for solving fullwave inverse scattering problems," *IEEE Trans. Antennas Propag.*, vol. 70, no. 8, pp. 6148–6159, 2022.
- [22] Y. Li, M. Tofighi, J. Geng, V. Monga, and Y. C. Eldar, "Efficient and interpretable blind image deblurring via algorithm unrolling," *IEEE Trans. Comput. Imaging*, vol. 6, pp. 666–681, 2020.
- [23] G. Revach, N. Shlezinger, X. Ni, A. L. Escoriza, R. J. G. van Sloun, and Y. C. Eldar, "Kalmannet: Neural network aided kalman filtering for partially known dynamics," *IEEE Trans. Signal Process.*, vol. 70, pp. 1532–1547, 2022.
- [24] S. B. Shah, P. Pradhan, W. Pu, R. Randhi, M. R. D. Rodrigues, and Y. C. Eldar, "Optimization guarantees of unfolded ISTA and ADMM networks with smooth soft-thresholding," *IEEE Trans. Signal Process.*, vol. 72, pp. 3272–3286, 2024.
- [25] Y. Yang, J. Sun, H. Li, and Z. Xu, "ADMM-CSNet: A deep learning approach for image compressive sensing," *IEEE Trans. Pattern Anal. Mach. Intell.*, vol. 42, no. 3, pp. 521–538, 2018.
- [26] V. Monga, Y. Li, and Y. C. Eldar, "Algorithm unrolling: Interpretable, efficient deep learning for signal and image processing," *IEEE Signal Process. Mag.*, vol. 38, no. 2, pp. 18–44, 2021.
- [27] Y. Ben Sahel, J. P. Bryan, B. Cleary, S. L. Farhi, and Y. C. Eldar, "Deep unrolled recovery in sparse biological imaging: Achieving fast, accurate results," *IEEE Signal Process. Mag.*, vol. 39, no. 2, pp. 45–57, 2022.
- [28] H. Zhou, T. Xie, Q. Liu, and S. Hu, "An augmented Lagrangian method-based deep iterative unrolling network for seismic full-waveform inversion," *IEEE Trans. Geosci. Remote Sens.*, vol. 62, pp. 1–13, 2024.
- [29] J. Adler and Ö. Öktem, "Learned Primal-dual Reconstruction," *IEEE Trans. Med. Imaging*, vol. 37, no. 6, pp. 1322–1332, 2018.
- [30] S. Deshmukh, A. Dubey, and R. Murch, "Unrolled optimization with deep learning-based priors for phaseless inverse scattering problems," *IEEE Trans. Geosci. Remote Sens.*, vol. 60, pp. 1–14, 2022.
- [31] M. Raissi, P. Perdikaris, and G. E. Karniadakis, "Physics-informed neural networks: A deep learning framework for solving forward and inverse problems involving nonlinear partial differential equations," *J. Comput. Phys.*, vol. 378, pp. 686–707, 2019.
- [32] R. Guo, T. Huang, M. Li, H. Zhang, and Y. C. Eldar, "Physics-embedded machine learning for electromagnetic data imaging: Examining three types of data-driven imaging methods," *IEEE Signal Process. Mag.*, vol. 40, no. 2, pp. 18–31, Mar. 2023.
- [33] T. Sharon and Y. C. Eldar, "Real-time model-based quantitative ultrasound and radar," *IEEE Trans. Comput. Imaging*, vol. 10, pp. 1175–1190, 2024.
- [34] S. Zumbo, S. Mandija, T. Isernia, and M. T. Bevacqua, "MiPhDUO: Microwave imaging via physics-informed deep unrolled optimization," *Inverse Problems*, vol. 40, no. 4, p. 045017, 2024.
- [35] N. Cohen, Y. Kovich, R. Guo, and Y. C. Eldar, "Deep unfolding of full waveform inversion for quantitative ultrasound imaging," *Proc. IEEE Int. Conf. Acoust., Speech, Signal Process. (ICASSP)*, Hyderabad, India, pp. 1–5, 2025.
- [36] G. Yao, N. V. da Silva, and D. Wu, "An effective absorbing layer for the boundary condition in acoustic seismic wave simulation," *J. Geophys. Eng.*, vol. 15, no. 2, pp. 495–511, Feb. 2018.
- [37] X. Yuan, et al., "Formulation and validation of Berenger's PML absorbing boundary for the FDTD simulation of acoustic scattering," *IEEE Trans. Ultrason. Ferroelectr. Freq. Control*, vol. 44, no. 4, pp. 816–822, Jul. 1997.
- [38] L. I. Rudin, S. Osher, and E. Fatemi, "Nonlinear total variation based noise removal algorithms," *Physica D: Nonlinear Phenomena*, vol. 60, no. 1–4, pp. 259–268, 1992.
- [39] S. Boyd, et al., "Distributed optimization and statistical learning via the alternating direction method of multipliers," *Found. Trends Mach. Learn.*, vol. 3, no. 1, pp. 1–122, 2010.
- [40] L. Deng, "The MNIST database of handwritten digit images for machine learning research [Best of the Web]," *IEEE Signal Process. Mag.*, vol. 29, no. 6, pp. 141–142, 2012.
- [41] F. A. Duck, "Physical Properties of Tissues: A Comprehensive Reference Book," Chapter 4, London, U.K.: Academic Press, 1990.
- [42] R. Courant, K. Friedrichs, and H. Lewy, "On the Partial Difference Equations of Mathematical Physics," *IBM J. Res. Dev.*, vol. 11, no. 2, pp. 215–234, 1967.
- [43] I. Ulrich, C. Boehm, P. Marty, N. Korta Martiartu, B. Lafci, X. L. Dean-Ben, D. Razansky, and A. Fichtner, "Waveform inversion with calibrated source-time functions for improving in-vivo ultrasound computed tomography," *Proc. SPIE Med. Imaging: Ultrasonic Imaging and Tomography*, vol. 12932, Art. no. 129320H, 2024.
- [44] D. P. Kingma and J. Ba, "Adam: A method for stochastic optimization," in *Proc. Int. Conf. Learn. Represent. (ICLR)*, San Diego, CA, USA, 2015.
- [45] R. Rau, D. Schweizer, V. Vishnevskiy, and O. Goksel, "Speed-of-sound imaging using diverging waves," *Int. J. Comput. Assist. Radiol. Surg.*, vol. 16, no. 7, pp. 1201–1211, 2021.
- [46] S. Ranjbaran, H. Aghamiry, A. Gholami, and S. Operto, "High-resolution speed of sound estimation from ultrasound waves using extended full wave inversion," in *Proc. SPIE*, vol. 11960, *Photons Plus Ultrasound: Imaging and Sensing*, Art. no. 119600V, 2022.
- [47] Y. Li, J. Wang, C. Su, W. Lin, X. Wang, and Y. Luo, "Quantitative ultrasound brain imaging with multiscale deconvolutional waveform inversion," *Chinese Phys. B*, vol. 32, no. 1, Art. no. 014303, 2023.